



HAL
open science

Sallaz et al. Hybrid all-solid-state thin film MSC based on quasi amorphous ALD TiO₂ electrode

Valentin Sallaz, Sylvain Poulet, Jean-Marc Boissel, Jouhaiz Rouchou, Yann Lamy, Frederic Voiron, Sami Oukassi

► To cite this version:

Valentin Sallaz, Sylvain Poulet, Jean-Marc Boissel, Jouhaiz Rouchou, Yann Lamy, et al.. Sallaz et al. Hybrid all-solid-state thin film MSC based on quasi amorphous ALD TiO₂ electrode. ACS Applied Energy Materials, 2022, 6 (1), pp.201-210. 10.1021/acsaem.2c02742 . cea-04528485

HAL Id: cea-04528485

<https://cea.hal.science/cea-04528485>

Submitted on 1 Apr 2024

HAL is a multi-disciplinary open access archive for the deposit and dissemination of scientific research documents, whether they are published or not. The documents may come from teaching and research institutions in France or abroad, or from public or private research centers.

L'archive ouverte pluridisciplinaire **HAL**, est destinée au dépôt et à la diffusion de documents scientifiques de niveau recherche, publiés ou non, émanant des établissements d'enseignement et de recherche français ou étrangers, des laboratoires publics ou privés.

Hybrid all-solid-state thin film microsupercapacitor based on quasi amorphous ALD TiO₂ electrode.

Valentin Sallaz^{a*}, Sylvain Poulet^b, Jouhaiz Rouchou^b, Jean-Marc Boissel^b, Isabelle Chevalier^b, Frédéric Voiron^a, Yann Lamy^b and Sami Oukassi^{b*}

^a*Murata Integrated Passive Solutions, 14000 Caen, France*

^b*Univ. Grenoble Alpes, CEA LETI Minatec Campus, 38054 Grenoble, France*

*Corresponding author

e-mail: sami.oukassi@cea.fr ; valentin.sallaz@murata.com

Abstract

In this work, nanometric (6-21 nm thick) quasi amorphous TiO_2 films have been elaborated and characterized in liquid and solid-state electrolyte (LiPON) half-cell architectures. For all considered configurations, the specific capacity extracted from cyclic voltammetry and galvanostatic cycling within [0.5-3V] potential range almost correspond to the theoretical value expected for the $\text{Li}_{x=1}\text{TiO}_2$ phase at low current density. Interestingly, TiO_2 films after LiPON deposition exhibited a constant initial amount of intercalated lithium ions independently of the different thicknesses and did not require a first activation process, in comparison to the liquid electrolyte configuration. Furthermore, the cooperative effects of high Li ion intercalation kinetics and low interfacial charge transfer resistance for 6nm TiO_2 electrode lead to an outstanding specific capacity of $2\text{mC}\cdot\text{cm}^{-2}$ at $1\mu\text{A}\cdot\text{cm}^{-2}$, and high rate performance with 60% capacity holding ratio at $100\mu\text{A}\cdot\text{cm}^{-2}$, thus highlighting the extrinsic pseudo-capacitive behavior of the sub 10nm electrodes.

A Li_xTiO_2 6nm/LiPON 100nm/Pt hybrid microsupercapacitor has been successfully fabricated achieving an operating voltage window of 3V and a specific capacity of $94\mu\text{F}\cdot\text{cm}^{-2}$ at $50\text{mV}\cdot\text{s}^{-1}$. In addition, the device also exhibited a 97% coulombic efficiency upon cycling for 10,000 continuous charge-discharge cycles. This work offers an approach to tune the Li ion storage properties of TiO_2 by nano-engineering and gives insights into the enhancement of pseudocapacitance-assisted lithium-storage capacity.

Keywords: amorphous TiO_2 ; asymmetric hybrid supercapacitor; thin film; all-solid-state; LiPON;

1. Introduction

In the perspective of a more connected and sustainable world, the extensive development of wireless sensor technologies or IoT requires always more miniaturized and on-chip integrated energy storage solutions [1]-[3]. If micro-batteries used to be one (if not the) essential element powering most of all electronic devices over the past decades [4], their limitation in terms of power density and lifespan have been the source of the emergence of high performance alternatives [5], [6]. In this regard, micro-supercapacitors (MSCs) appear as one of the most promising power sources to simultaneously meet high energy and power densities (compared to conventional dielectric capacitors and batteries respectively) and long term cycle life [7].

On-chip MSCs integration enables miniaturization and a fabrication complexity reduction of the whole system. Therefore, fabrication techniques like PVD, ALD or else must be compatible with semi-conductor and MEMS technology and the active materials - electrodes and the electrolyte - require high areal or volumetric performances. Lithium phosphorous oxinitride (LiPON), which is well known for its great advantages in terms of thermal and electrochemical stabilities [8], has recently been reported as promising thin solid ions conductor when integrated in 2D parallel plate on-chip electrical double layer microsupercapacitors (MSCs) [9]. The devices were obtained based on standard semi-conductor fabrication techniques and exhibited a power density of $6.8 \mu\text{W}\cdot\text{cm}^{-2}$ and an energy density of $68 \text{nWh}\cdot\text{cm}^{-2}$ on more than 100.000 reversible cycles. As the authors mentioned however, the MSCs stacking was designed as a test vehicle, and improvements must be brought to boost the energy density.

Asymmetric Hybrid Microsupercapacitors (AsHMSCs) introduce a charge storage mechanism based on both electric double-layer phenomena and faradaic reaction, using respectively capacitive-type and insertion-type electrodes. Literature usually reports these insertion-type electrodes as either a battery-type electrode (e.g. $\text{Li}_4\text{Ti}_5\text{O}_{12}$ [10], $\text{Ni}(\text{OH})_2$ [11]) or a pseudocapacitive material that store energy through fast reversible redox reaction (e.g. conductive polymers [12], metal-oxides [13], [14]...). This construction allows to increase the energy density (with both specific capacity and operating voltage), thus filling the gap between MSCs and microbatteries [15]. Within this context, the selection of electrode materials and their interaction at the electrolyte interface is a key issue to optimize the AsHMSC electrochemical performance.

TiO_2 as negative electrode material has arouse a great academic interest for sustainable Li-ions based MSCs. Abundant and stable, TiO_2 film is easy to fabricate and the lithiation of Li_xTiO_2 up to $x = 1$ corresponds to a maximum theoretical capacity of $336 \text{mAh}\cdot\text{g}^{-1}$ [16]. Among all known TiO_2 structures and polymorphs [17], [18], several including amorphous TiO_2 phase was reported to demonstrate

pseudocapacitive properties [19], [20], such as a quasi linear potential variation with the state of charge (SoC) (within [0.5 - 2V] vs Li⁺/Li range) and fast rate capabilities, making it an interesting candidate for increasing the energy density of MSCs.

To study the benefits of amorphous TiO₂ electrode in a LiPON-based AsHMSC structure, an initial evaluation of nanometric TiO₂ was carried out in both liquid and solid-state electrolyte (LiPON) half-cell configurations. The impact of the solid LiPON/TiO₂ interface as well as the different Li ion intercalation kinetics of all TiO₂ thicknesses were evidenced, exhibiting the pseudocapacitive behavior of the sub 10nm electrodes. The integration of 6nm TiO₂ film within an all-solid-state Pt/TiO₂/LiPON/Pt structure enabled to obtain a high specific capacitance of 95 μF.cm⁻² within a 3V voltage range obtained at 50 mV.s⁻¹, and more than 10.000 successful continuous charge-discharge cycles. This work offers an approach to tune the Li ion storage properties of TiO₂ by nano-engineering and gives insights into the enhancement of pseudocapacitance ion-storage capacity.

2. Experimental

2.1. Materials

200mm Si wafers with Si_3N_4 (160nm) and SiO_2 (100nm) were used as substrate upon which were previously deposited and patterned Ti 50nm/Pt 250nm bilayer (Alcatel-600 tool). Pt electrode was used as bottom current collector known as a blocking electrode [9]. Thin TiO_2 films were deposited by ALD (Cambridge-Savannag tool) using tetrakis dimethylamido titanium ($\text{Ti}(\text{N}(\text{CH}_3)_2)_4$ or TDMAT) and water precursors at 80°C. Pulse and purges times used for depositions were respectively 450ms and 10s for TDMAT, 80ms and 15s for H_2O and sequences of 71, 142 and 284 cycles were performed to obtain 6, 11 and 21nm films respectively confirmed by spectroscopic ellipsometry (**Figure S1**).

On the first part of the study, half-cells were realized by depositing a 100nm LiPON film as solid-state electrolyte by rf-magnetron sputtering of $\text{Li}_3\text{PO}_4\text{-Li}_2\text{O}$ (65% - 35% molar ratio) target under N_2 reactive atmosphere (Endura PVD tool) and an evaporated Li electrode (1 μm) through shadow masks. For comparison, half-cells in liquid configuration were also assembled using Li foil (Rockwood Lithium GmbH, 135 μm thickness) as reference and counter electrode, placed as close as possible to the working electrode. The electrolyte was a 1:1:3 mixture by volume of ethylene carbonate (EC), propylene carbonate (PC) and dimethyl carbonate (DMC) containing LiPF_6 1M. The use of a polypropylen sheet and Celgard 2400 separator between both electrodes enabled to prevent from lithium dendrites formation upon cycling. An illustrated description is given in **Figure S2**.

On a second part, a Ti/Pt/ TiO_2 /LiPON/Pt stack was fabricated using a 250nm top Pt counter electrode to form the AsHMSC structure as shown in **Figure 1b**. The active area of the samples was comprised between 20 and 45 mm^2 .

2.2. Characterization methods

Cross sectional observations of the AsHMSC were carried out using a transmission electron microscope (TEM) coupled with focused ion beam (FIB) and the structure of TiO_2 films was investigated by high resolution TEM (HR-TEM).

The chemistry of the AsHMSC structure was obtained with a time-of-flight scanning ion mass spectrometer (TOF-SIMS). The samples were profiled using a 2 keV Cs^+ sputtering beam over rastered area of 150x150 μm^2 and a 25 keV Bi^{3+} analysis beam over analyzed area of 40x40 μm^2 , below -100°C to immobilize Li ions. The elemental distribution of Li, P, O, N and Ti was visualized by $^7\text{LiCs}^{2+}$, $^{16}\text{Cs}^{2+}$, $^{31}\text{PCs}^{2+}$, $^{14}\text{NCs}^{2+}$ and $^{22}\text{TiCs}^{2+}$ secondary ions.

Electrochemical Impedance Spectroscopy (EIS), cyclic voltammetry (CV) and galvanostatic charge and discharge (GCPL) experiments were conducted at room temperature using a VMP3 multipotentiostat (BioLogic) coupled with the EC-Lab software.

3. Results and discussion

3.1. Characterization of TiO₂ electrode

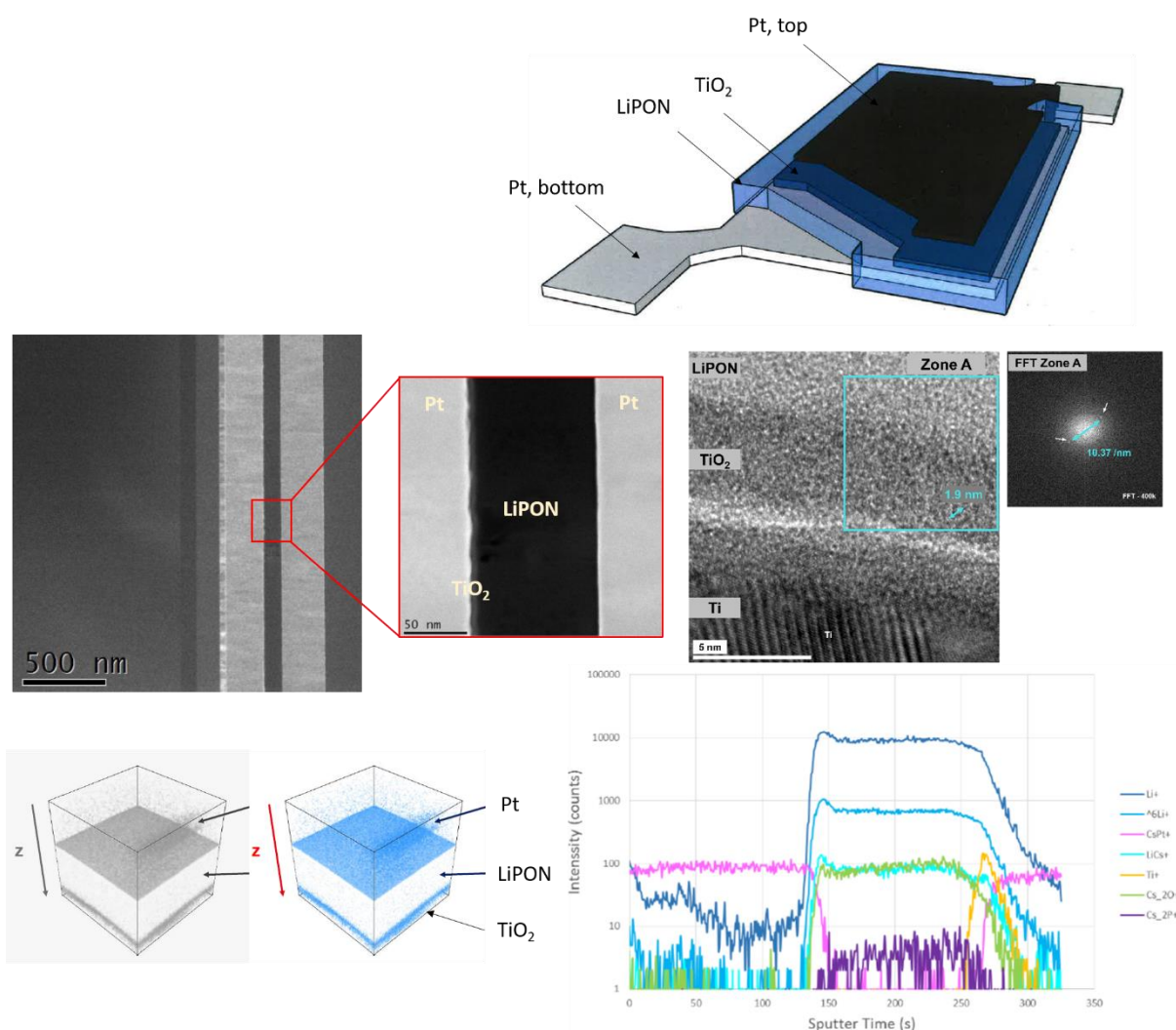


Figure 1. (a) Schematic representation of fabricated AsHMSC. (b) Photo of the fabricated devices. (c) Cross sectional TEM observation of AsHMSC device. (d) HR-TEM images captured with magnification of 400k: nano crystallites around 2 nm in size have been found embedded inside TiO₂ amorphous matrix. (e) Depth profile analysis of AsHMSC stack. (f) 3D elemental mapping of Li and Ti elements enabled by TOF-SIMS.

A cross-sectional TEM image of the fabricated devices is shown in **Figure 1c**. Each layer appears continuous, homogeneous and presents smooth interfaces with no delamination or local blisters, which indicates good adhesion at the various interfaces. TiO₂ and LiPON films thicknesses are ~6nm and 110nm respectively and matches with the intended values.

The 6nm-TiO₂ microstructure was characterized using high resolution transmission electron microscopy (HR-TEM). As seen in **Figure 1d**, the results confirmed that the synthesized film is mostly amorphous.

However, by doing local FFT in comparison with Si substrate reference (**Figure S3**), some spots are observed in the diffractogram (underlined by white arrows) and an interplanar spacing of lattice fringe of 0.207nm (i.e. $d^* = 10.37\text{nm}^{-1}$ in the reciprocal space) is determined corresponding to the (210) crystal phase of rutile TiO_2 [21]. Although rutile phase is generally obtained at very high temperature ($> 800^\circ\text{C}$ [22]), the presence of nano-inclusions of rutile phase within as-formed ALD films has already been reported elsewhere depending on the nature of the substrate or the set of precursors used [23], [24].

TOF-SIMS analysis was performed next on the AsHMSC. A uniform distribution of Li, P, O and N elements is observed along LiPON film thickness (**Figure 1e**), and the 3D elemental mapping provided in **Figure 1f** reveals that Li element is notably present within TiO_2 film (that will be discussed later).

Finally, the composition of the TiO_2 film determined by XPS (**Figure S4**). Ti is essentially in the form of Ti^{4+} (97%) and we calculate an O/Ti ratio of 1.94 indicating an excellent stoichiometry of the as-deposited film. However, carbon and nitrogen contamination are present (1.3% and 1.0% respectively), likely originating from partially removed $-\text{N}(\text{CH}_3)_2$ ligands due to low operating deposition temperature.

3.2. Electrochemical characterization of Pt/ TiO_2 electrode in liquid and solid-state half-cell: initial state of charge and activation process

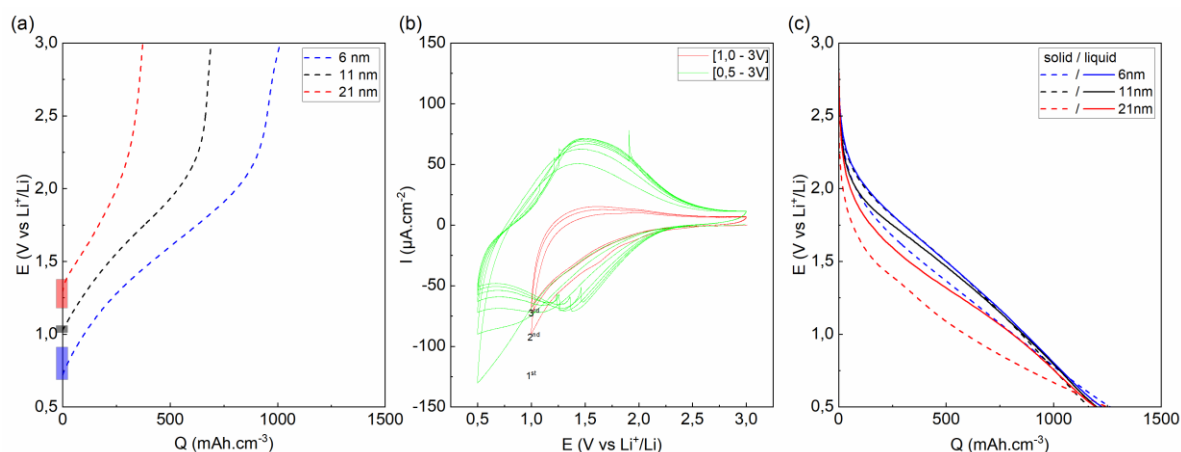


Figure 2. (a) First charge curve for 6, 11 and 21nm TiO_2 films in contact with LiPON. (b) First ten CV cycles within [1 - 3V] followed by ten cycles within [0.5 - 3V] for 21nm TiO_2 in liquid half-cell. (c) Comparison of the 10th discharge curve in liquid and LiPON half-cell configuration for the three TiO_2 thicknesses ($I = 1 \mu\text{A}\cdot\text{cm}^{-2}$).

The following part will focus on the electrochemical behavior of single TiO_2 electrodes implemented in half-cell configuration, using LiPF_6 and LiPON as liquid and solid-state electrolyte respectively, and Li as reference electrode.

The Open Circuit Voltage (OCV) of both configuration was systematically measured before each electrical test in order to evaluate the potential initial Li intercalation "x" in Li_xTiO_2 . Interestingly, we obtained 1.3V, 1V and 0.8V in average for 21, 11 and 6nm TiO_2 films integrated with LiPON respectively, whereas the OCV was centered around 3V for all oxides thickness in liquid cell. These differences suggest that an initial amount of lithium was already inserted in the oxide layer in the presence of LiPON. Capacities of 345, 650 and 1010 mAh.cm^{-3} can be extracted upon first charge step (**Figure 2a**) which lead to surface charge capacity of $0.66 \mu\text{Ah.cm}^{-2}$ (= 2.4 mC.cm^{-2}) in average and correspond to a state-of-charge (SoC) of 27, 51 and 79% for 21, 11 and 6nm electrodes respectively. These results demonstrate the existence of a surface pre-lithiation of bottom electrodes during LiPON deposition, under process that still needs to be understood (reducing environment, thermal diffusion, or other). This observation corroborates the previous result obtained by TOF-SIMS analysis in **Figure 1f**.

Focusing now on the first discharge step in liquid cell, it is interesting to observe through cyclic voltammetry measurements that no clear cathodic and anodic peaks appeared while cycling first within [1 - 3V] vs Li^+/Li range, without any impact of subsequent cycles on the CV shape (**Figure 2b**). Changes in the CV behavior only occurred when sweeping down to 0.5V with:

- (1) an (irreversible) increase of the cathodic current resulting in a discharge capacity of 2250 mAh.cm^{-3} (i.e. implying a Li fraction into Li_xTiO_2 of $x \sim 1.8$) (**Figure S5**).
- (2) the appearance of a broad oxidation peak between 1.2V and 1.8V and, inversely, a reduction peak at 1.5V vs Li^+/Li .

Such behavior has already been reported for ALD amorphous TiO_2 cycled in liquid configuration as an "activation" process [25], [26]. Although the mechanism remains unclear, few works suggested that phase transition to cubic $\text{Li}_2\text{Ti}_2\text{O}_4$ of a small fraction of amorphous TiO_2 occurs during the first lithiation step [27]-[29]. Conversion reactions between Li-ions and micro-clusters or non-stoichiometric TiO_2 spatially distributed within the whole films might also be considered in correlation with the first irreversible (volumetric) discharge capacity.

The potential discharge profiles of all configuration after 10 cycles of stabilization are given in **Figure 2c**. We observe that the curves are shifted towards lower potential values for $\text{TiO}_2/\text{LiPON}$ interface or thicker TiO_2 films, likely resulting from charge transfer mechanism or ohmic drop. In the present study, this does not seem to significantly impact the value of the discharge capacity at low rates ($I = 1 \mu\text{A.cm}^{-2}$), which is extracted in average around 1200 mAh.cm^{-3} for all configurations. This fits with the $\text{Li}_{0.95}\text{TiO}_2$ formula intended for amorphous phase and suggests here an almost complete transformation of Ti^{4+} into Ti^{3+} .

3.3. Charge storage phenomena and transport properties in TiO₂

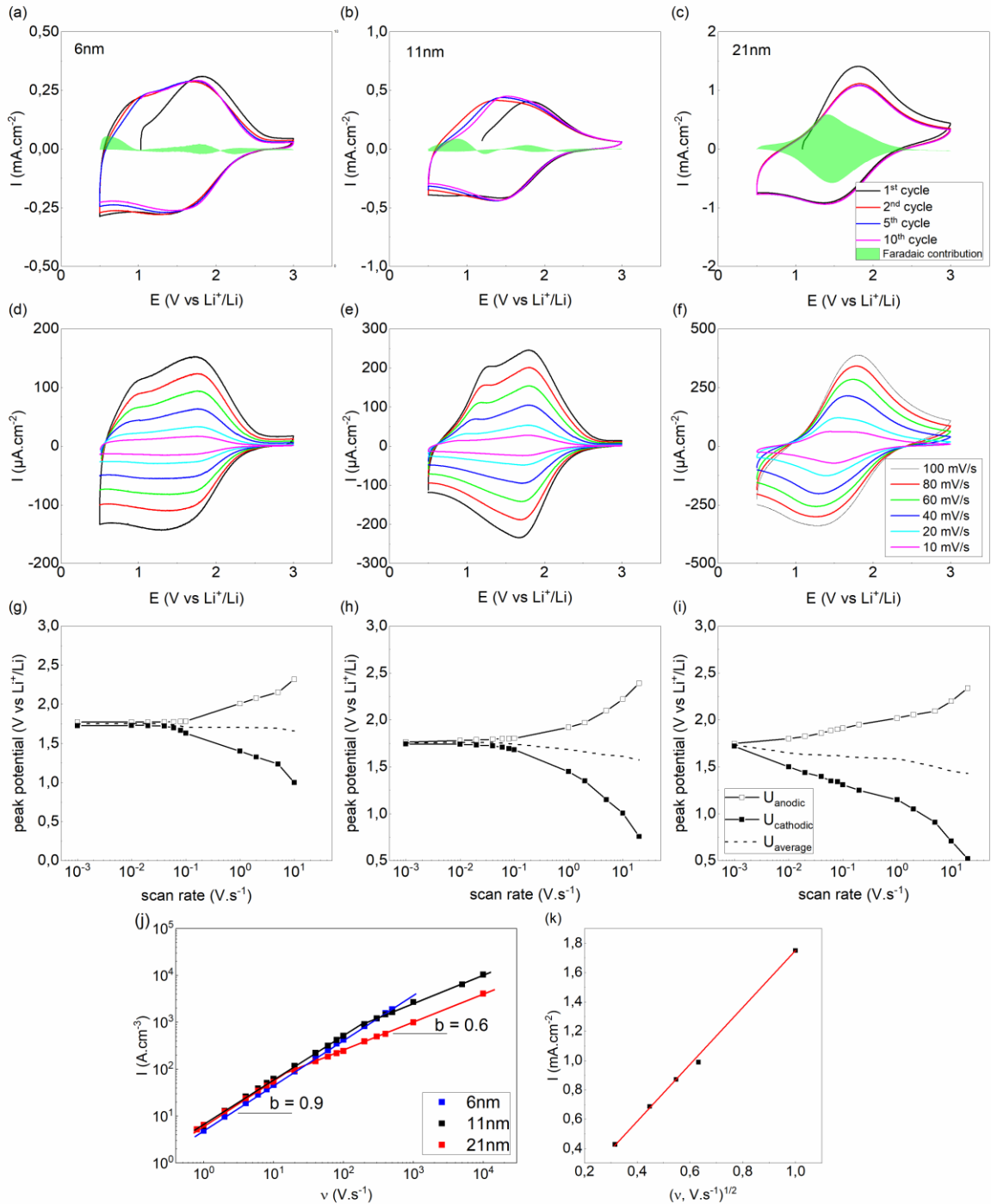


Figure 3. (a, b, c) 10th first CV cycles plotted at 200mV·s⁻¹ for 6nm, 11nm and 21nm TiO₂ films respectively including Faradaic contribution to overall signal. (d, e, f) CV plotted for scan rates between 10 and 100 mV·s⁻¹ for 6nm, 11 and 21nm films respectively. (g, h, i) Peaks potential shift as function of the scan rate for 6nm, 11 and 21nm films respectively. (j) Current oxidation peak density plotted as

function of the scan rates. (k) Oxidation peak I_{peak} vs \sqrt{v} for 21nm TiO_2 .

Reversibility of Li-ion extraction in contact with LiPON upon first charge step is discussed based on CV measurements within [0.5 - 3V] range (**Figures 3a, b and c**). The main Li extraction potential is centered around 1.75V vs Li^+/Li with similar broad potential distributions as observed in liquid cell (see in **Figure S6a, b and c**). This feature is commonly accepted for amorphous TiO_2 phase deposited by ALD which presents a high amount of defects and Li insertion/extraction sites at various redox potentials [30]. Identical current density levels are observed for both anodic and cathodic scans for each TiO_2 thickness. No significant change appears between the first and subsequent cycles. Particularly, no electrical signature of the previously observed activation step is seen here, suggesting that LiPON deposition already enabled the TiO_2 films activation. Similar experiments with scan rates varying from 10 to 100 $\text{mV}\cdot\text{s}^{-1}$ were carried out and presented in **Figures 3d, e and f**. A shift of main oxidation and reduction peaks towards higher and lower potential values respectively is observed when increasing both the scan rate and TiO_2 film thickness (**Figures 3g, h and i**), which is usually related to overpotential caused by charge transfer or ohmic resistances of the electrolyte and/or electrodes. Besides, the average peak potential given by $U_{\text{av}} = (U_{\text{anodic}} + U_{\text{cathodic}})/2$ also slightly decreases indicating a less favorable lithiation kinetics in comparison to delithiation. Experiments in liquid configuration (**Figure S6c, d and e**) exhibit similar CV shape, current levels and peak potential variations implying that LiPON does have an (significant) impact on the cell transport properties. It is also worth noticing the presence of a second redox peak at lower oxidation potential which participates to the overall capacity. This peak appears kinetically less favorable than the main reaction as more strongly subject to overpotential, up to the point that both peaks are almost combined for 21nm TiO_2 film at high rate. A better observation of this peak is given in **Figure S7** for a scan rate of 1 $\text{mV}\cdot\text{s}^{-1}$. However, no clue allowed us to determine at this time the nature of this reaction.

CV experiments also enables to observe the contribution of diffusion limited processes to overall capacity. **Figure 3j** presents plots of the peak current densities variation with the scan rate v from 1 $\text{mV}\cdot\text{s}^{-1}$ to 10 $\text{V}\cdot\text{s}^{-1}$ for the main anodic peak. The current density variation with v is commonly assumed to obey a power law and can be written as [31]:

$$I = a \cdot v^b \quad (3.1)$$

where a and b are adjustable coefficients. The exponent b is comprised between 0.5 and 1, which corresponds to semi-infinite diffusion process and an ideal capacitor behavior respectively. From the log-log plot, two regions can be observed depending on the TiO_2 thickness: a low rate with $b = 0.9$ corresponding to a surface limited storage mechanism and a diffusion limited charge at higher scan rates with $b = 0.6$. The volumetric current appears to be thickness independent but

the transition between the two regions varies while increasing the thickness: this substantiates the extrinsic pseudocapacitive behavior of amorphous TiO₂ [32], where lithium insertion/extraction is not kinetically limited by semi-infinite diffusion of Li-ions due to extremely small dimensions.

Accordingly, and focusing on the diffusion limited high scan rates region of 21nm TiO₂ films (i.e. between 100 mV.s⁻¹ and 1 V.s⁻¹), the faradaic contribution is assumed to follow approximately the Randles-Sevcik equation [31]:

$$I_p \approx 268600 \cdot z^2 \cdot \sqrt{D_{Li}} \cdot C_{Li} \cdot \sqrt{v} \quad (3.2)$$

with I_p the peak current density (A.cm⁻²), z the valance of charge carrier (= +1 for Li-ions), D_{Li} the the apparent diffusion coefficient (cm².s⁻¹), v the scan rate (V.s⁻¹) and C_{Li} the Li concentration into TiO₂.

The Li concentration into TiO₂ is calculated from the maximum capacity obtained as 0.0464 mol.cm⁻³. The peak current densities extracted from CV measurements are plotted as function of square-root of the scan rate in **Figure 3k**. An almost linear variation with \sqrt{v} is observed, enabling the calculation of Li diffusion coefficient from the slope as $2 \cdot 10^{-14}$ cm².s⁻¹ \pm 3%. This model does not consider any ohmic drop effects induced by the peak potential shift when increasing the scan rate, and thus ignores possible changes in Li-ions exchanged quantities ($b = 0.6$ indicates a deviation from the Randles-Sevcik equation which could be explained by C_{Li+} variation with the scan rate). Notwithstanding, this result remains in the range of values previously reported in the literature for amorphous TiO₂ materials in liquid configuration [26], [32], [33], as solid-state configuration at this scale does not induce any further limitation related to diffusion in TiO₂ electrode.

For similar diffusion properties, the decrease of the TiO₂ thickness would enable a reduction of both Li diffusion path and electronic resistance improving the rate capability. Thus, by combining the high storage capacity of the amorphous phase and the pre-lithiation effect enabled by LiPON deposition, the 6nm-TiO₂ film meets the necessary requirements for pseudocapacitive electrode integrated in ASHMSC configuration.

3.4. Rate capability of a-TiO₂ electrode

To investigate the Li ion diffusion properties into amorphous TiO₂ for different thicknesses, galvanostatic cycling was performed at a soft charge current density of 1 μ A.cm⁻² with various discharge current densities from 1 to 1000 μ A.cm⁻². **Figure 4** depicts results of different rate performances of the 6, 11 and 21nm thin TiO₂ films. For 1 μ A.cm⁻² discharge current, the three films exhibit capacities of 0.7, 1.2 and

2.2 $\mu\text{Ah}\cdot\text{cm}^{-2}$ respectively, corresponding to the geometrical factor between the different thicknesses. By increasing the discharge rate, the gap between the three films is significantly reduced up to the point where the capacity of 21nm thin TiO_2 becomes lower than 6nm TiO_2 films. Specifically, the obtained capacity at discharge current density of $1\text{ mA}\cdot\text{cm}^{-2}$ represents 62.5, 64.1 and 14.4% of the initial capacity (at $1\text{ }\mu\text{A}\cdot\text{cm}^{-2}$), which confirms that the 21nm TiO_2 film presents lower rate performance than the thinner films. As observed, the Coulombic efficiency is around 99.7% for 6nm and 11nm films indicating the excellent reversibility of Li-ions insertion and extraction. For 21nm films however, the efficiency decreases as the discharge current increases caused by the poor reaction kinetics. Last, one can observe that there is almost no variation in capacity when applying back low charge current density, substantiating that the use of alternate high and low rates (i) does not impact the reaction reversibility and (ii) that capacity decay is mostly related to kinetic limitations.

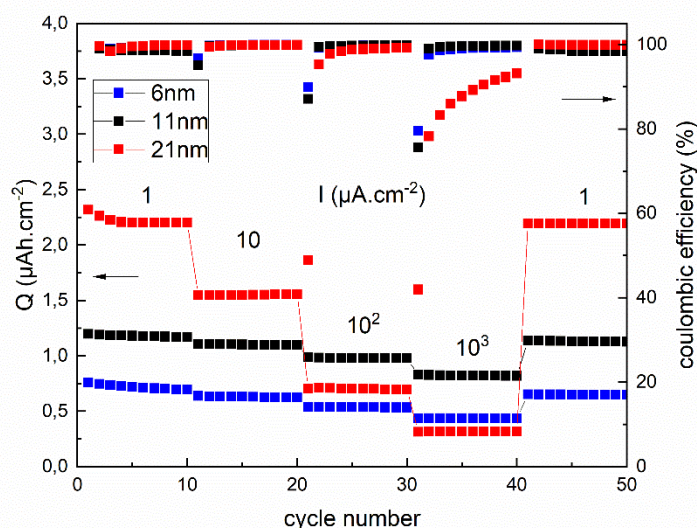


Figure 4. (a) Discharge capacity of 6, 11 and 21nm TiO_2 films and (b) coulombic efficiency as function of the discharge rate.

3.5. Towards high performance hybrid asymmetric MSC

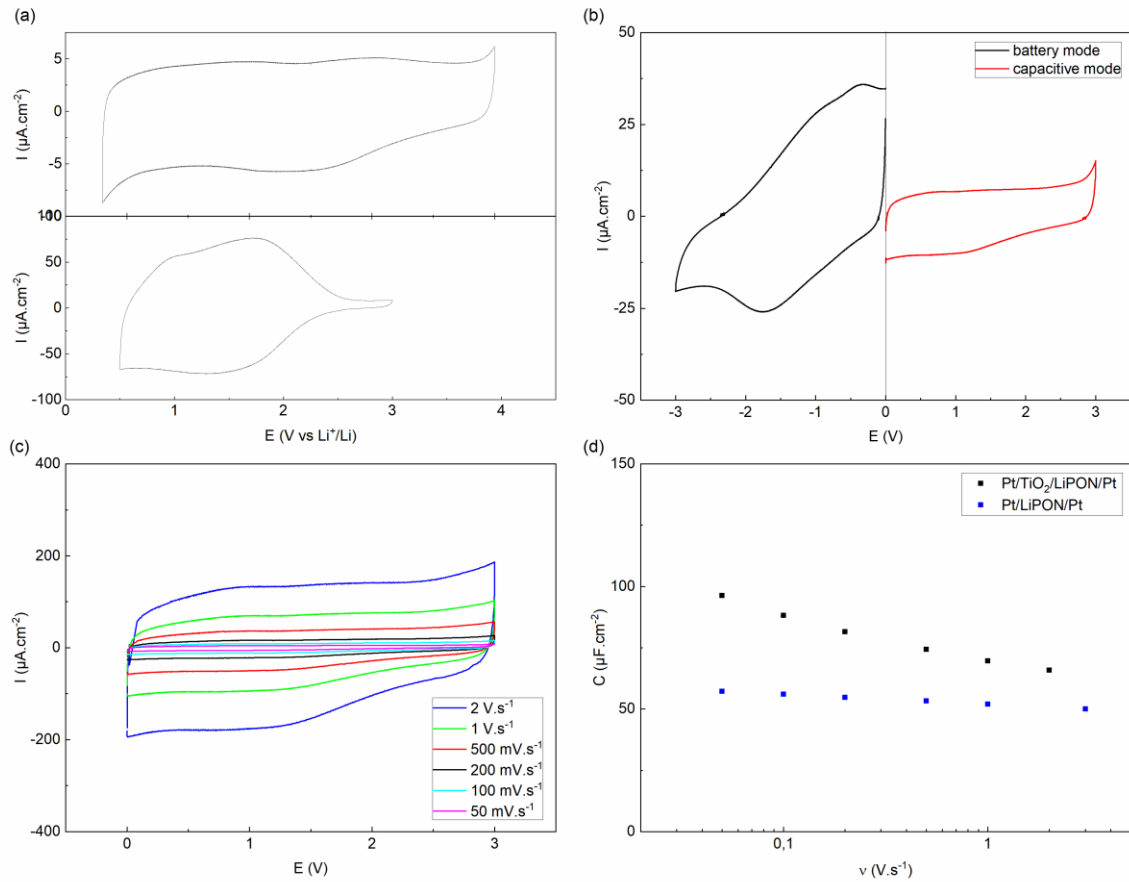


Figure 5. (a) CV curves of Pt/LiPON/Li (top) and 6nm-TiO₂/LiPON/Li (bottom) half-cells at 100 mV.s⁻¹. (b) CV curves of Pt/LiPON/TiO₂ cell with positive (red curve) and negative bias (black curve) at 100 mV.s⁻¹. (c) CV curves of AsHMSC plotted for scan rates between 50 mV.s⁻¹ and 2 V.s⁻¹. (d) Extracted capacitance from CV curves plotted as function of the scan rate and compared with Pt/LiPON/Pt MSC.

The respective behaviors of 6nm-TiO₂ and Pt electrodes, recorded in half-cell solid configuration and presented in **Figure 5a**, enables to understand the overall behavior of the cell. The principle of AsHMSC is, by applied a positive bias at the Pt electrode, to make use of the double layer Pt/LiPON interface capacity within its whole stability range (i.e. 1V to 4V vs Li⁺/Li) while TiO₂ is operating around its broad lithiation peak. This behavior is thus obtained in **Figure 5b** (red curve) sharing with Pt/LiPON/Li half-cell (obtained in previous work) similar box like shape of the CV curve within [0 - 3V] voltage range and a capacitance around 90 μF.cm⁻² extracted for a scan rate of 100 mV.s⁻¹ [9]. Note that inversely by application of negative bias (**Figure 5b**, black curve), the device no longer acts as a capacitor but as a low performance "battery" implying Li-Pt alloying reactions on the Pt side (black curve). As seen in **Figure 5c**, the reversible CV shape remains almost unchanged when increasing the scan rate from 50 mV.s⁻¹ to 2 V.s⁻¹ and the different capacitances extracted from CV (plotted as function of the scan rate in **Figure 5d**) demonstrates well

the beneficial effect of adding an interfacial pseudocapacitive electrode to boost the capacitance density compared to Pt/LiPON/Pt MSCs. Nevertheless, a 28% decrease of the capacitance value is observed when increasing the cycling rate by 2 orders of magnitude, which can be explained by the impact of the high internal resistance related to amorphous TiO_2 film (known as a bad electronic conductor with a band gap around 3.0 - 3.4 eV). The kinetic limitation would imply a shift of the Li insertion peak (on the negative electrode) from its thermodynamic value when cycled at high rate, and consequently an efficiency loss of the AsHMSC behavior. This observation is consistent with Conway's recommendation suggesting that AsHMSCs should not be cycled with speed rate exceeding 1C [15].

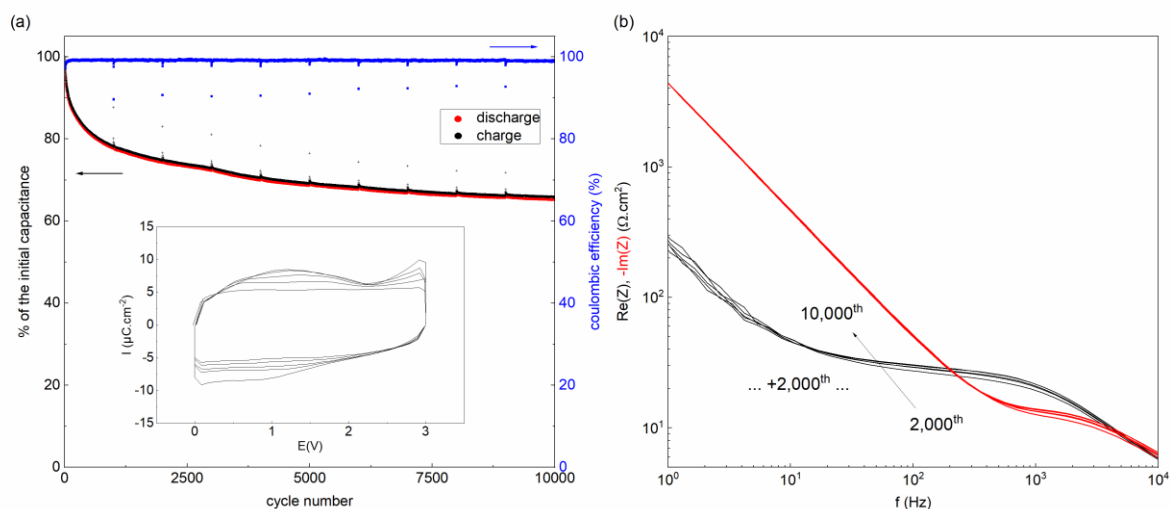


Figure 6. (a) Cycle life of AsHMSC over 10,000 cycles at $10 \mu\text{A}\cdot\text{cm}^{-2}$ (Inset: dQ vs E). (b) Evolution of the AsHMSC impedance spectra (real and imaginary parts) with cycling.

Finally, AsHMSC endurance was tested by applying a constant charge/discharge current of $10 \mu\text{A}\cdot\text{cm}^{-2}$ between 0 and 3V (**Figure 6a**). The device exhibits a 97% coulombic efficiency even after cycling for 10,000 continuous charge-discharge cycles. An initial capacitance drop of $\sim 18\%$ is observed however during the first five hundreds cycles followed by a smoother decay of $2.10^{-3} \%$ /cycle in average for the following cycles. The derivative signal of the charge and discharge profiles (**Figure S8**) given in the inset is losing intensity in its entirety while cycling, however no second contribution to the impedance signal is seen (**Figure 6b**). This only comes with a very slight increase of the internal resistance of $1.10^{-3} \%$ /cycle suggesting the TiO_2 film remains stable over cycling, and thus that the capacitance loss would be more related to an increase of the overpotential on the TiO_2 side during lithiation (previously observed as less favorable than delithiation).

4. Conclusion

In this work, we have introduced a thin pseudocapacitive electrode to enhance the electrochemical performance of Pt/LiPON/Pt MSC described in previous work. Amorphous TiO_2 films, tested in liquid and solid-state (using LiPON) half-cell configurations, provides similar results in terms of storage capacity, typically 95% of the theoretical capacity. Interestingly, TiO_2 films after LiPON deposition exhibits an initial amount of lithium almost constant for all considered thickness and do not require a first activation process, contrary to the liquid configuration. The broad potential distribution in addition to excellent rate capability properties for ultrathin films highlighted the extrinsic pseudocapacitive behavior of amorphous TiO_2 material.

A thin 6nm- TiO_2 films has been implemented in AsHMSC configuration as insertion electrode facing a Pt electrode that sustains a double layer type storage mechanism. The device exhibits capacitance value of around $94 \mu\text{F}\cdot\text{cm}^{-1}$ at $50 \text{ mV}\cdot\text{s}^{-2}$ which is about twice higher than Pt/LiPON/Pt MSC and a good endurance of 10.000 cycles as expected for such configuration. However, this comes with a high and fast decrease of capacitance upon cycling, as well as moderate rate properties that seems to originate from an increase of the overpotential during the lithiation step particularly.

Although we succeeded to design high performance AsHMSC, improvements are still necessary to increase the cycling stability and the cycling rate. The development of ALD layers for electrodes and the electrolyte (sub 50nm) would enable a decrease of the internal resistance by decreasing significantly the whole stack thickness, and certainly a better control of the pre-lithiation by introducing lithiated precursors during the TiO_2 ALD deposition.

References

- [1] D. Chen, Z. Lou, K. Jiang, and G. Shen, "Device Configurations and Future Prospects of Flexible/Stretchable Lithium-Ion Batteries," *Adv. Funct. Mater.*, vol. 28, no. 51, pp. 1-21, 2018.
- [2] A. González, E. Goikolea, J. A. Barrena, and R. Mysyk, "Review on supercapacitors: Technologies and materials," *Renew. Sustain. Energy Rev.*, vol. 58, pp. 1189-1206, 2016.
- [3] C. García Núñez, L. Manjakkal, and R. Dahiya, "Energy autonomous electronic skin," *npj Flex. Electron.*, vol. 3, no. 1, 2019.
- [4] S. Oukassi *et al.*, "Millimeter scale thin film batteries for integrated high energy density storage," *Tech. Dig. - Int. Electron Devices Meet. IEDM*, vol. 2019-December, pp. 618-621, 2019.
- [5] J. Ni, A. Dai, Y. Yuan, L. Li, and J. Lu, "Three-Dimensional Microbatteries beyond Lithium Ion," *Matter*, vol. 2, no. 6, pp. 1366-1376, 2020.
- [6] K. M. Abraham, "Prospects and limits of energy storage in batteries," *J. Phys. Chem. Lett.*, vol. 6, no. 5, pp. 830-844, 2015.
- [7] N. A. Kyeremateng, T. Brousse, and D. Pech, "Microsupercapacitors as miniaturized energy-storage components for on-chip electronics," *Nat. Nanotechnol.*, vol. 12, no. 1, pp. 7-15, 2016.
- [8] X. Yu, J. B. Bates, G. E. Jellison Jr., and F. X. Hart, "A Stable Thin-Film Lithium Electrolyte: Lithium Phosphorus Oxynitride," *J. Electrochem. Soc.*, vol. 144, no. 2, pp. 524-532, 1997.
- [9] V. Sallaz, S. Oukassi, F. Voiron, R. Salot, and D. Berardan, "Assessing the potential of LiPON-based electrical double layer microsupercapacitors for on-chip power storage," *J. Power Sources*, vol. 451, 2020.
- [10] G. G. Amatucci, F. Badway, A. Du Pasquier, and T. Zheng, "An Asymmetric Hybrid Nanoaqueous Energy Storage Cell," *J. Electrochem. Soc.*, vol. 148, no. 8, pp. 930-939, 2001.
- [11] J. Yan *et al.*, "Advanced asymmetric supercapacitors based on Ni(OH)₂/graphene and porous graphene electrodes with high energy density," *Adv. Funct. Mater.*, vol. 22, no. 12, pp. 2632-2641, 2012.
- [12] A. M. Bryan, L. M. Santino, Y. Lu, S. Acharya, and J. M. D'Arcy, "Conducting Polymers for Pseudocapacitive Energy Storage," *Chem. Mater.*, vol. 28, no. 17, pp. 5989-5998, 2016.
- [13] V. Augustyn *et al.*, "High-rate electrochemical energy storage through Li + intercalation pseudocapacitance," *Nat. Mater.*, 2013.
- [14] V. Augustyn, P. Simon, and B. Dunn, "Pseudocapacitive oxide materials for high-rate electrochemical energy storage," *Energy Environ. Sci.*, vol. 7, no. 5, 2014.
- [15] W. G. Pell and B. E. Conway, "Peculiarities and requirements of asymmetric capacitor devices based on combination of capacitor and battery-type electrodes," vol. 136, pp. 334-345, 2004.
- [16] S. Goriparti, E. Miele, F. De Angelis, E. Di Fabrizio, R. Proietti Zaccaria, and C. Capiglia, "Review on recent progress

- of nanostructured anode materials for Li-ion batteries," *J. Power Sources*, vol. 257, pp. 421-443, 2014.
- [17] J. Shen, H. Wang, Y. Zhou, N. Ye, G. Li, and L. Wang, "Anatase/rutile TiO₂ nanocomposite microspheres with hierarchically porous structures for high-performance lithium-ion batteries," *RSC Adv.*, vol. 2, no. 24, pp. 9173-9178, 2012.
- [18] A. G. Dylla, G. Henkelman, and K. J. Stevenson, "Lithium Insertion in Nanostructured TiO₂ (B) Architectures," *Acc. Chem. Res.*, vol. 46, no. 5, pp. 1104-1112, 2013.
- [19] T. Brousse and B. Daniel, "To Be or Not To Be Pseudocapacitive?," *J. Am. Chem. Soc.*, vol. 162, no. 5, pp. 5185-5189, 2015.
- [20] H. Wang, G. Jia, Y. Guo, Y. Zhang, H. Geng, and J. Xu, "Atomic Layer Deposition of Amorphous TiO₂ on Carbon Nanotube Networks and Their Superior Li and Na Ion Storage Properties," 2016.
- [21] F. Scarpelli, T. F. Mastropietro, T. Poerio, and N. Godbert, "Mesoporous TiO₂ Thin Films: State of the Art," in *Titanium Dioxide - Material for a Sustainable Environment*, 2018.
- [22] C. Byrne, R. Fagan, S. Hinder, D. E. McCormack, and S. C. Pillai, "New approach of modifying the anatase to rutile transition temperature in TiO₂ photocatalysts," *RSC Adv.*, vol. 6, no. 97, pp. 95232-95238, 2016.
- [23] A. T. Iancu, M. Logar, J. Park, and F. B. Prinz, "Atomic layer deposition of undoped TiO₂ exhibiting p-type conductivity," *ACS Appl. Mater. Interfaces*, vol. 7, no. 9, pp. 5134-5140, 2015.
- [24] J. Pointet, P. Gonon, L. Latu-Romain, A. Bsiesy, and C. Vallée, "Rutile-structured TiO₂ deposited by plasma enhanced atomic layer deposition using tetrakis(dimethylamino)titanium precursor on in-situ oxidized Ru electrode," *J. Vac. Sci. Technol. A Vacuum, Surfaces, Film.*, vol. 32, no. 1, p. 01A120, 2014.
- [25] M. Xie et al., "Amorphous Ultrathin TiO₂ Atomic Layer Deposition Films on Carbon Nanotubes as Anodes for Lithium Ion Batteries," *J. Electrochem. Soc.*, vol. 162, no. 6, pp. A974-A981, 2015.
- [26] S. Moitzheim, S. De Gendt, and P. M. Vereecken, "Investigation of the Li-Ion Insertion Mechanism for Amorphous and Anatase TiO₂ Thin-Films," *J. Electrochem. Soc.*, vol. 166, no. 2, pp. A1-A9, 2019.
- [27] Q. Gao et al., "Direct evidence of lithium-induced atomic ordering in amorphous TiO₂ nanotubes," *Chem. Mater.*, vol. 26, no. 4, pp. 1660-1669, 2014.
- [28] A. Auer, D. Steiner, E. Portenkirchner, and J. Kunze-Liebhäuser, "Nonequilibrium Phase Transitions in Amorphous and Anatase TiO₂ Nanotubes," *ACS Appl. Energy Mater.*, vol. 1, no. 5, pp. 1924-1929, 2018.
- [29] D. Steiner, A. Auer, E. Portenkirchner, and J. Kunze-Liebhäuser, "The role of surface films during lithiation of amorphous and anatase TiO₂ nanotubes," *J. Electroanal. Chem.*, vol. 812, no. November 2017, pp. 166-173, 2018.
- [30] J. Feng, B. Yan, M. O. Lai, and L. Li, "Design and Fabrication of an All-Solid-State Thin-Film Li-Ion Microbattery with Amorphous TiO₂ as the Anode," *Energy Technol.*, vol. 2, no. 4, pp. 397-400, 2014.
- [31] H. Lindström et al., "Li⁺ ion insertion in TiO₂ (anatase). 2.

- Voltammetry on nanoporous films," *J. Phys. Chem. B*, vol. 101, no. 39, pp. 7717-7722, 1997.
- [32] J. Ye *et al.*, "Amorphization as a Pathway to Fast Charging Kinetics in Atomic Layer Deposition-Derived Titania Films for Lithium Ion Batteries," *Chem. Mater.*, vol. 30, no. 24, pp. 8871-8882, 2018.
- [33] Y. Jiang *et al.*, "Evidence for Fast Lithium-Ion Diffusion and Charge-Transfer Reactions in Amorphous TiO₂ Nanotubes: Insights for High-Rate Electrochemical Energy Storage," *ACS Appl. Mater. Interfaces*, vol. 10, no. 49, pp. 42513-42523, 2018.

Conflicts of interest

There are no conflicts to declare.

Supplementary Information

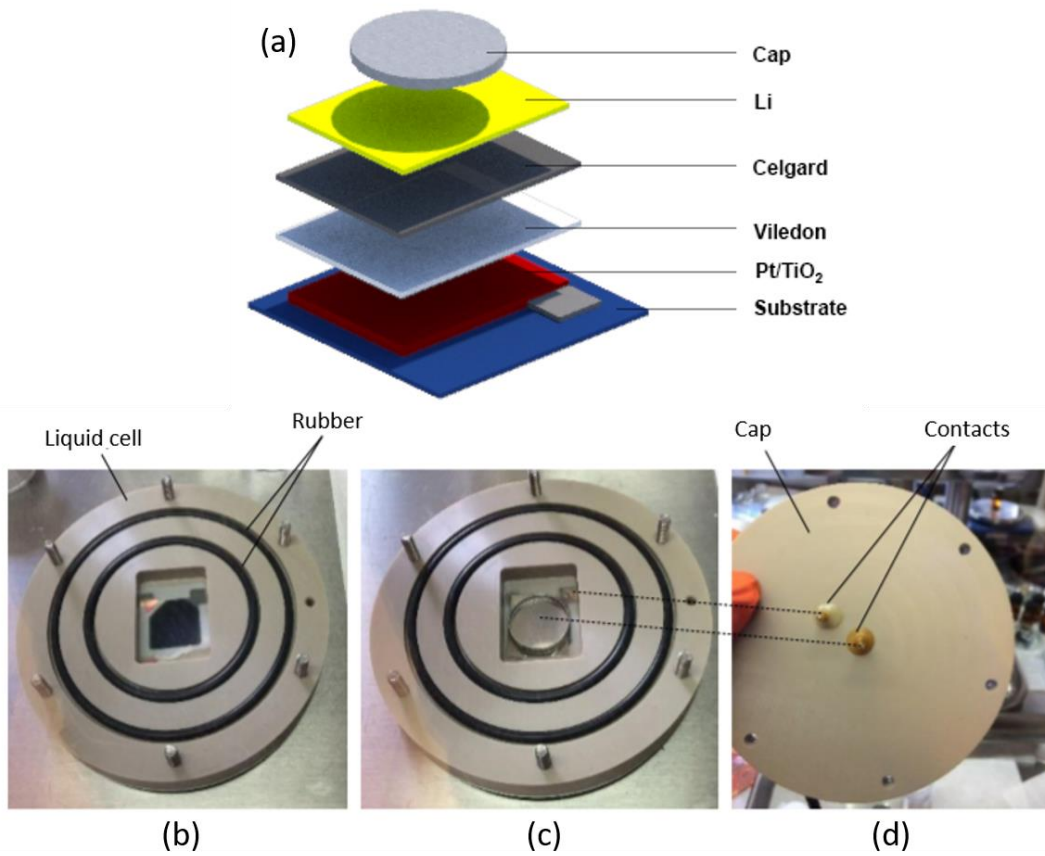


Figure S1: Photos of liquid cell assembly: (a) stack, (b) substrate laid into the cell, (c) separators, Li foil and metal cap placed onto the substrate, (d) cover with positive and negative contacts.

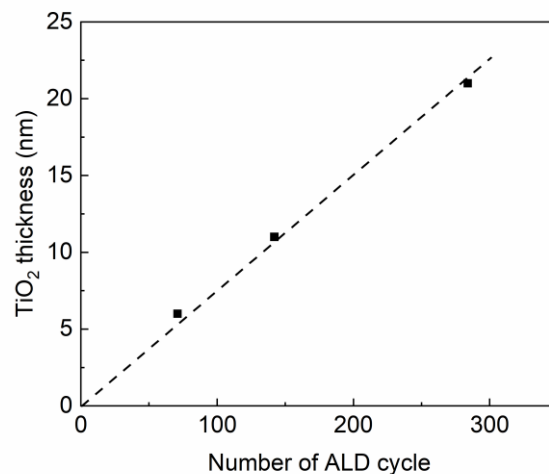


Figure S2. Growth of ALD TiO₂ films; thickness is obtained by SE.

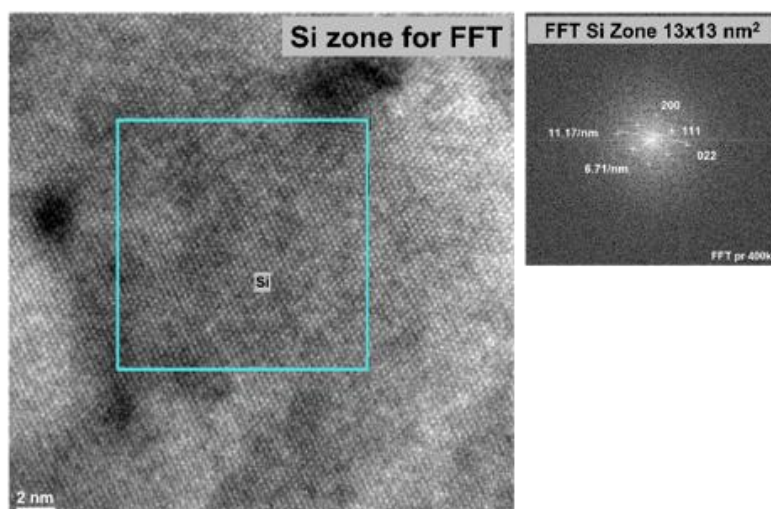


Figure S3. HR-TEM reference image of Si substrate captured with magnification of 400k.

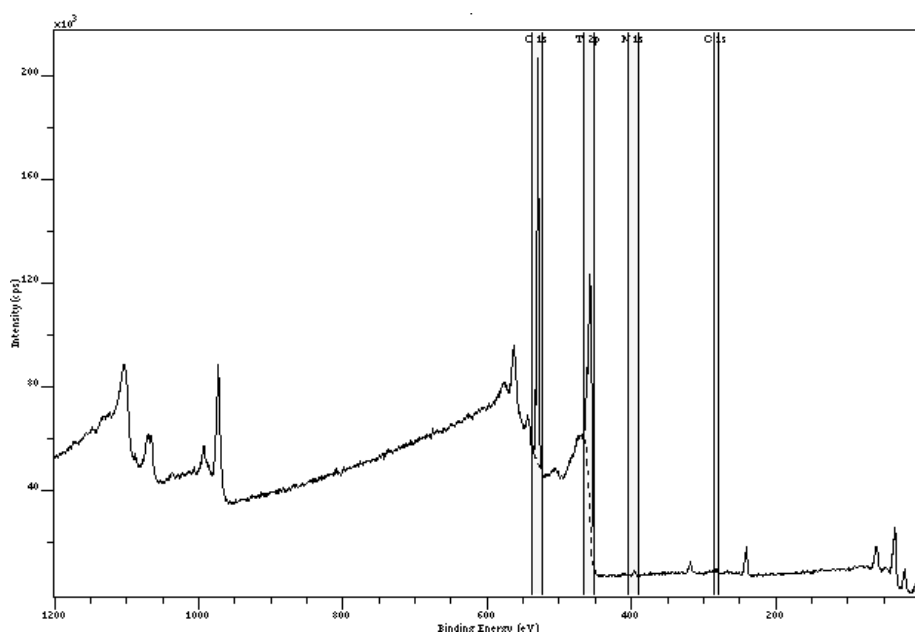


Figure S4: XPS survey spectra of TiO₂ film.

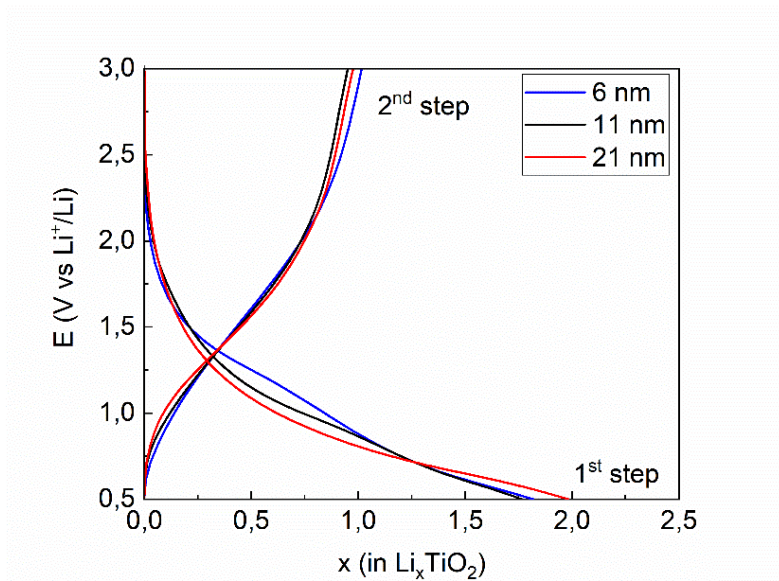


Figure S5: First discharge followed by first charge (1st and 2nd cycle) of thin TiO₂ cycled in liquid cell within [0.5 – 3V] potential range vs Li⁺/Li at 1 $\mu\text{A}\cdot\text{cm}^{-2}$.

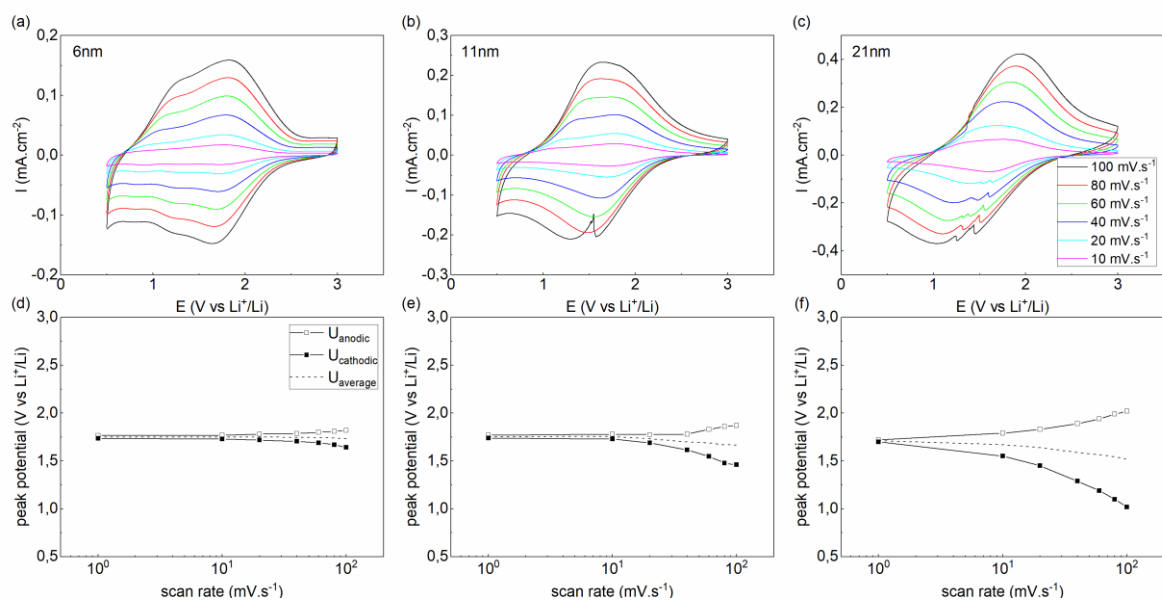


Figure S6. (a, b, c) CV plotted for scan rates between 10 and 100 $\text{mV}\cdot\text{s}^{-1}$ for 6nm, 11 and 21nm films respectively in liquid half-cell configuration. (d, e, f) Peaks potential shift as function of the scan rate for 6nm, 11 and 21nm films respectively.

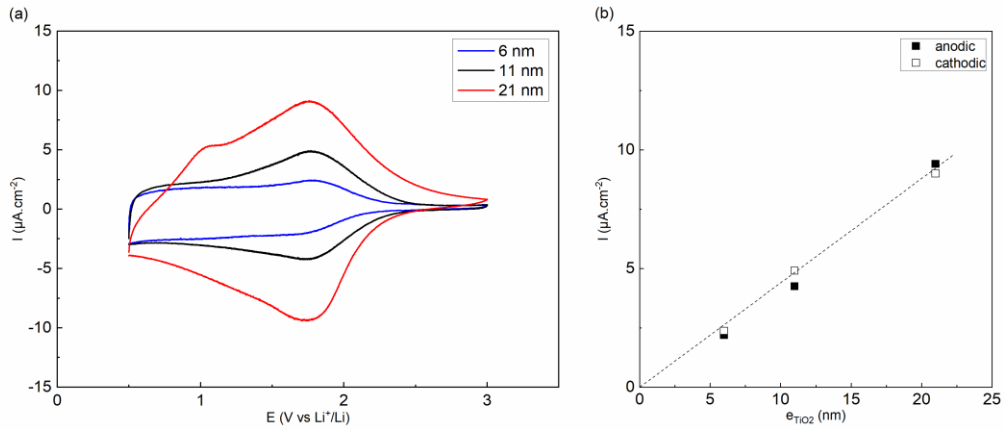


Figure S7. CV profiles of 6nm, 11nm and 21nm TiO₂ films at a scan rate of 1 mV.s⁻¹. (Inset: I_{peak} vs TiO₂ thickness).

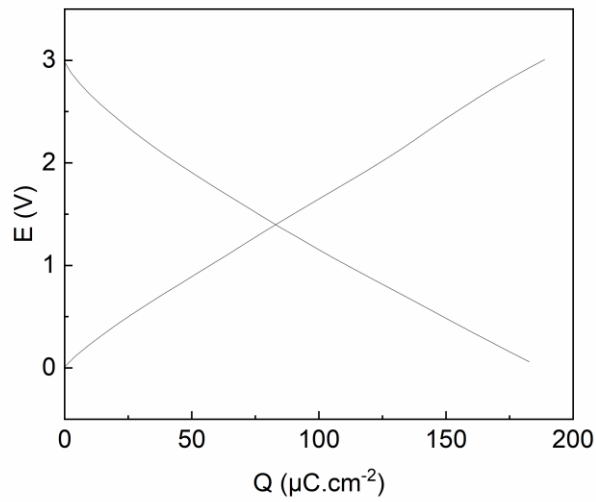


Figure S8: 10,000th charge and discharge profile with constant current of 10 $\mu\text{A}\cdot\text{cm}^{-2}$.